

2  
3 **APPLICATIONS OF THREE-DIMENSIONAL BOX MODELING TO**  
4 **PALEONTOLOGICAL FUNCTIONAL ANALYSIS**  
5

6 IMRAN A. RAHMAN<sup>1</sup> AND STEPHAN LAUTENSCHLAGER<sup>2</sup>

7 <sup>1</sup>Oxford University Museum of Natural History, Parks Road, Oxford OX1 3PW, UK

8 <imran.rahman@oum.ox.ac.uk>

9 <sup>2</sup>School of Earth Sciences, University of Bristol, Life Sciences Building, 24 Tyndall Avenue,  
10 Bristol BS8 1TQ, UK <glzsl@bristol.ac.uk>

11  
12 **ABSTRACT.**—Functional analysis through computer modeling can inform on how extinct  
13 organisms moved and fed, allowing us to test long-standing paleobiological hypotheses.  
14 Many such studies are based on digital models derived from computed tomography or surface  
15 scanning, but these methods are not appropriate for all fossils. Here, we show that box  
16 modeling — 3-D modeling of complex shapes based on simple objects — can be used to  
17 reconstruct the morphology of various fossil specimens. Moreover, the results of  
18 computational functional analyses utilizing such models are very similar to those for models  
19 derived from tomographic or surface-based techniques. Box modeling is more broadly  
20 applicable than alternative methods for digitizing specimens, and hence there is great  
21 potential for this approach in paleontological functional analysis. Possible applications  
22 include large-scale comparative studies, analyses of hypothetical morphologies, and virtually  
23 restoring incomplete/distorted specimens.

24  
25 **INTRODUCTION**

Computational methods for the three-dimensional (3-D) visualization and analysis of fossils are becoming a mainstay of paleontology (Cunningham et al., 2014; Sutton et al., 2014, in press). The application of tomographic techniques, especially computed tomography (CT) and its variants (e.g., micro-CT and synchrotron CT), has allowed researchers to describe fossils in unprecedented detail, providing new insights into anatomy (e.g., Garwood and Dunlop, 2011; Giles et al., 2015; Porro et al., 2015), behavior (e.g., Witmer et al., 2003; Zelenitsky et al., 2009; Lautenschlager et al., 2012), development (e.g., Rücklin et al., 2012; Schmidt et al., 2013; Rahman et al., 2015a), and taphonomy (e.g., Smith et al., 2009; Cunningham et al., 2012; Rahman et al., 2015b). In addition, surface-based methods such as photogrammetry and laser scanning are enabling the rapid digitization of surface topography and texture at distance, making them particularly well suited to difficult-to-access mounted museum specimens (e.g., Bates et al., 2009; Falkingham, 2012) and field sites (e.g., Breithaupt et al., 2004; Bates et al., 2008). These approaches have facilitated the reconstruction of high-resolution 3-D models of fossils, which can be subjected to quantitative functional analyses, informing tests of hypotheses pertaining to the paleobiology of extinct organisms (e.g., Rayfield, 2005; Shiino et al., 2012; Lautenschlager, 2014; Rahman et al., 2015c).

This new ‘virtual world of paleontology’ has enormous potential for studies of fossil functional morphology (Rayfield, 2007; Anderson et al., 2011a; Cunningham et al., 2014). However, it is not always feasible to digitally reconstruct a 3-D model of a specimen that can be used as the basis for such analyses. Access to instruments and/or software can be difficult or prohibitively expensive — although this is increasingly being offset by the development of cheap digitization methods (e.g., photogrammetry) and freely-available software (e.g., Drishti, Limaye, 2012; SPIERS, Sutton et al., 2012; VisualSFM, Wu, 2013). Additionally, it

might not be possible to obtain permission to use tomographic or surface-based methods to digitize fossils held in some museum or private collections. In a few cases, important type specimens have been lost (Smith et al., 2006), making them unavailable for study. Lastly, a single specimen that fully captures the 3-D morphology of the living organism might not be known; methods for digitally restoring the original form of fossils do exist (e.g., Gunz et al., 2009; Cunningham et al., 2014; Lautenschlager, in press), but cannot be applied in all cases and are often highly subjective. These obstacles have limited the widespread application of methods for paleontological functional analysis.

Box modeling is an alternative way of creating 3-D digital models of fossils that overcomes the difficulties outlined above. It involves the repeated addition and modification of simple shapes, such as cubes, cylinders, or spheres, to produce a final model (Hess, 2010). The accuracy of this process is aided by virtually fitting the model to reference images of the object of interest in multiple views. Open-source software for box modeling exists (e.g., Blender), meaning the approach can be used to create digital models for free (apart from hardware costs). Furthermore, this method does not necessarily rely on access to a single perfectly-preserved specimen, as the models can be based on published scientific reconstructions derived from the study of multiple specimens. Thus far, the approach has been used predominantly for visualization (e.g., Stein, 2010; Haug et al., 2011; Haug et al., 2014), but there is also potential utility for analyses of functional morphology. Herein, we present a case study of box modeling and functional analysis applied to three different fossil taxa. Models were generated using box modeling and compared to existing 3-D reconstructions based on CT or photogrammetry. The functional performance of these models was then analyzed using finite-element analysis (FEA) or computational fluid dynamics (CFD), and the results were evaluated for each pair of models.

76  
77  
78  
79  
80  
81  
82  
83  
84  
85  
86  
87  
88  
89  
90  
91  
92  
93  
94  
95  
96  
97  
98  
99  
100

**MATERIAL AND METHODS**

**Construction of 3-D models**

We selected three different specimens, which vary in terms of their morphological complexity, size, and taxonomic group. These were: 1) The skull of the theropod dinosaur *Allosaurus fragilis* (MOR 693); 2) a dorsal vertebra of the ornithischian dinosaur *Stegosaurus stenops* (NHMUK R36730); and 3) a complete individual of the cinctan echinoderm *Protocinctus mansillaensis* (MPZ 2004/170). The original specimens are housed in the Museum of the Rockies, Bozeman, Montana (MOR), the Natural History Museum, London (NHMUK), and the Museo Paleontológico de la Universidad de Zaragoza, Spain (MPZ), respectively.

Box modeling was performed in Blender v. 2.73 (<http://www.blender.org>). Blender is an open-source 3-D computer graphics program that has been used in paleontology for preparing high-quality images and animations (e.g., Garwood and Dunlop, 2011; Giles et al., 2015; Rahman et al., 2015a, b), estimating musculoskeletal constraints (Lautenschlager, 2015), and box modeling (e.g., Stein, 2010; Haug et al., 2011; Haug et al., 2014). Hess (2010) provides a detailed introduction to the software and Garwood and Dunlop (2014) includes a user guide aimed at paleontologists.

Published photographs (*Stegosaurus*, Maidment et al., 2015, fig. 22) or scientific reconstructions (*Allosaurus*, Madsen, 1976, plates 1, 2; *Protocinctus*, Rahman and Zamora, 2009, fig. 3) of the specimens in different orientations (lateral, dorsal, and ventral for *Allosaurus*; lateral, frontal, dorsal, ventral, and caudal for *Stegosaurus*; and dorsal and frontal for *Protocinctus*) were imported into Blender (Properties Shelf → Add Image) to use as a

reference to guide box modeling. Next, a base object was created from the Blender mesh objects library; in all cases, a cube (Fig. 1A) was selected (shift + A → Cube) because of its simple and adaptable geometry. The cube was subdivided using loop cuts (ctrl + R) to increase the number of elements (Fig. 1B), and individual components of the cube (vertices and edges) were fitted to the outline of the reference image in different views by translation (selected components moved by the same amount in one or more directions; shortcut G), rotation (selected components turned by the same amount around one or more axes; shortcut R), and scaling (selected components increased/decreased in size by the same amount in one or more directions; shortcut S) (Fig. 1C, D). Additional elements were then added in different orientations by extruding existing elements (selected components duplicated; shortcut E) to form other parts of the object (Fig. 1E–G). Further details were modeled by translating individual vertices or edges to match the reference images (Fig. 1H). As a final step, the resolution (i.e., number of elements in each model) was increased by applying a subdivision surface modifier (Properties Editor → Object Modifiers → Subdivision surface). This gave the final models a smoother exterior surface, but did not appreciably alter their general morphology (Supplemental Data 1, 3, 5). A Windows desktop PC with 8 GB RAM and a 2 GB Intel HD graphics card was used for modeling; the time taken was ~300 minutes for the *Allosaurus* skull, ~120 minutes for the *Stegosaurus* vertebra, and ~30 minutes for the *Protocinctus* fossil.

Virtual reconstructions of the same three specimens were used for comparison. The *Allosaurus* skull was scanned using a medical CT scanner at the Bozeman Deaconess Hospital, Bozeman, Montana and digitally reconstructed using Avizo v. 8.1 (<http://www.fei.com/software/avizo3d>) (see Rayfield et al., 2001; Lautenschlager, 2015 for details). The *Stegosaurus* vertebra was digitized with photogrammetry using a standard

digital SLR camera and visualized in 3D using VisualSFM v. 0.5.26 (<http://ccwu.me/vsfm>) (see Brassey et al., 2015 for details). The *Protocinctus* fossil was scanned using a Phoenix v|tome|x s micro-CT system at Imperial College London and digitally reconstructed using SPIERS v. 1.10 (<http://spiers-software.org>) (see Rahman and Zamora, 2009 for details). The resulting reconstructions were subjected to weak smoothing in Blender (Properties Editor → Object Modifiers → Smooth) to minimize surface noise (Supplemental Data 2, 4, 6).

### **Comparison of 3-D models**

The open-source point-cloud and mesh processing software CloudCompare v. 2.6.2 (<http://www.danielgm.net/cc>) was used to quantitatively compare the 3-D models generated using box modeling to the corresponding ones based on CT or photogrammetry. Pairs of models were opened in CloudCompare, scaled to the same size (rostromaxillary length for *Allosaurus*, vertebral height for *Stegosaurus*, and thecal length for *Protocinctus*), and aligned to their respective centers of gravity using the match bounding-box centers method. Where necessary, these alignments were adjusted manually by translating and rotating the models so they were superimposed on top of one another. The models were then finely registered using the iterative closest point algorithm. Distance measurements were calculated automatically and the results were exported as false-color contour plots of the distances between elements for each pair of models.

### **Finite-element analysis**

FEA was used to reconstruct stresses for the models of *Allosaurus* and *Stegosaurus*. The pairs of models were scaled to the same surface area and imported into HyperMesh v. 11.0 (<http://www.altairhyperworks.com/product/HyperMesh>) to create solid finite-element models of suitable resolution (~500,000 four-noded tetrahedral elements for the *Allosaurus* skull and

~250,000 four-noded tetrahedral elements for the *Stegosaurus* vertebra). Because it is impossible to accurately quantify the structure of bone in extinct organisms, the material properties of alligator mandibular cortical bone (Young's modulus  $E = 20.49$  GPa, Poisson's ratio  $\nu = 0.40$ ; Zapata et al., 2010) were assigned to the models as an analogy for dinosaur bone (Lautenschlager et al., 2013). The material was treated as isotropic and homogeneous, which has been shown to be a reasonable assumption for comparisons among taxa (Gil et al., 2015). The *Allosaurus* models were constrained from rigid body motion at the quadrates (eight constraints on each side) and the occipital condyle (10 constraints). Arbitrary but physiologically realistic muscle forces were applied to two nodes (500 N each) at the squamosal on both sides to simulate contraction of the jaw adductor muscles. In addition, a force of 1500 N was applied to the first maxillary tooth to simulate biting at this tooth position. The *Stegosaurus* models were constrained from rigid body motion on the anterior and posterior surfaces of the vertebral centrum (10 nodes each). The models were loaded with arbitrary forces (100 N each) applied to the neural spine and the tips of the transverse processes to simulate muscle forces. All models were imported into ABAQUS v. 6.14 (<http://www.3ds.com/products-services/simulia/products/abaqus>) for analysis and post-processing. Results were visualized as false-color contour plots of average Von Mises stresses, in addition to measurements of Von Mises stresses, deformation, and minimum/maximum principal strain for selected points along the models.

## **Computational fluid dynamics**

CFD was used to analyze fluid flow around the two models of *Protocinctus*. CFD simulations were performed using COMSOL Multiphysics v. 5.1 (<https://uk.comsol.com/>). The computational domain consisted of a three-dimensional half-cylinder (220 mm in length and 64 mm in diameter), with the *Protocinctus* models fixed on the lower boundary. Three-

dimensional, incompressible flow of water (density  $\rho = 1025 \text{ kg/m}^3$ , dynamic viscosity  $\mu = 1.002 \text{ mPa}\cdot\text{s}$ ) was simulated with a uniform inlet velocity of  $0.2 \text{ m/s}$  (Reynolds number  $\sim 2000$ ) at the upstream end and a zero-pressure outlet at the downstream end. Slip conditions were assigned to the top and sides of the half-cylinder, simulating flow through the domain; no-slip conditions were assigned to the lower boundary of the half-cylinder and the interface between the fluid and the fossil, fixing the fluid velocity at zero. The domain was meshed using free tetrahedral elements, with a minimum element size of  $0.90 \text{ mm}$  and a maximum element size of  $3.02 \text{ mm}$ . The shear-stress transport turbulence model was used to solve the Reynolds-averaged Navier-Stokes equations and a stationary solver was used to compute the steady-state flow patterns. Results were exported as false-color contour plots of velocity magnitude and downstream velocity profiles.

For comparison with the CFD simulations, experimental analyses of water flow were carried out using a life-size 3-D printed model of *Protocinctus*. The model was glued to a bed of coarse sediment at the bottom of a recirculating hydraulic flume ( $8.5 \text{ m}$  in length,  $0.3 \text{ m}$  in width, and  $0.3 \text{ m}$  in depth), which had a flow velocity of  $\sim 0.2 \text{ m/s}$ . A two-component DANTEC fiber-optic laser Doppler anemometry system was used to measure flow velocity downstream of the model. See Rahman et al. (2015c) for full details. Additionally, to further investigate the influence of surface geometry on the results, a CFD simulation was carried out using a three-dimensional rectangle with the same length, width, and height as the *Protocinctus* models (other modeling parameters identical to those outlined above).

## RESULTS

### 3-D models



The general shape of the models produced using box modeling and CT/photogrammetry was broadly similar (Fig. 2; Supplemental Data 1–6), but the number of elements making up each model varied depending on the approach taken and the morphological complexity of the original specimen. For *Allosaurus*, the model generated using box modeling had 200,144 elements (faces), whereas the model based on CT had 179,961 elements (10.08% difference). For *Stegosaurus*, the model generated using box modeling had 225,344 elements, whereas the model based on photogrammetry had 409,912 elements (81.90% difference). For *Protocinctus*, the model generated using box modeling had 25,088 elements, whereas the model based on micro-CT had 110,802 elements (341.65% difference).

The results of the CloudCompare analysis revealed that there were noticeable differences between the models generated with box modeling versus those based on CT or photogrammetry, which are indicated by regions of blue or orange in the false-color distance plots (Fig. 3). In particular, the back of the skull of *Allosaurus*, the neural spine and the transverse processes of *Stegosaurus* (together with the lamina along these structures), and the anterior and upper surfaces of *Protocinctus* showed clear mismatches (i.e., relatively large distances between corresponding elements in the pair of models). Moreover, the deviation between each pair of models was not consistent. For *Allosaurus*, there was a 12.74% difference in surface area and a 30.52% difference in volume between the two models. For *Stegosaurus*, there was a 1.19% difference in surface area and a 0.98% difference in volume between the two models. For *Protocinctus*, there was a 9.31% difference in surface area and a 2.57% difference in volume between the two models.

## **Finite-element analysis**

Based on a visual comparison of the results, it was evident that the distribution of Von Mises stresses was generally very similar for the box-modeled dinosaurs and the corresponding models derived from CT/photogrammetry (Fig. 4). For the *Allosaurus* model, the majority of stress hot-spots occurred in the same locations in both models. The model derived from CT showed a few additional stress hot-spots or regions of elevated stress magnitude around the anteroventral braincase region, the external naris, and parts of the skull roof. These corresponded to the regions where the CT-based model exhibited more detail. Stress magnitudes and peak stresses were very similar in both models. Similarly, the *Stegosaurus* models showed a very close correspondence in terms of the distribution and magnitude of Von Mises stresses. Stress hot-spots were almost identical in both models. Furthermore, quantitative comparison of Von Mises stresses, deformation, and minimum/maximum principal strain for selected points revealed a very close match between the 3-D models of fossils generated using box modeling (dotted lines in Fig. 5) and those based on CT or photogrammetry (solid lines in Fig. 5).

### **Computational fluid dynamics**

Visual inspection of the results showed that the two models of *Protocinctus* produced very similar flow patterns (Fig. 6A–D), which consisted of an elongate, low-velocity wake downstream of *Protocinctus* and steep velocity gradients immediately upstream of and above the model (the boundary layer). The wake was more symmetrical for the box-modeled *Protocinctus*, reflecting the less asymmetrical outline of this model (compared to the one based on micro-CT). The thickness of the boundary layer was approximately the same for both models.

Comparison of the downstream velocity profiles for the two computational models of *Protocinctus* revealed a very close correspondence at all positions and heights within the flow domain (red circles and green triangles in Fig. 6E–H). The results of the flume tank experiment were broadly similar within ~5 mm of the lower boundary of the domain (i.e., within the boundary layer), but the velocity measurements became increasingly different as the height increased (blue triangles in Fig. 6E–H). Conversely, the results of the CFD simulation for the three-dimensional rectangle were rather different in the regions closest to the model (i.e., height < 5 mm; 0 mm and 10 mm downstream), and did not become similar to the other computer models until well above the base of the domain (magenta boxes in Fig. 6E–H).

## DISCUSSION

The 3-D models generated with box modeling were broadly similar to those based on CT/photogrammetry, but showed obvious differences in certain aspects of their geometry (Fig. 2; Supplemental Data 1–6). This was clear in the results of the CloudCompare analysis (Fig. 3). There is no relationship between the number of elements used and the similarity of the models; *Allosaurus* showed the greatest variation between the models in terms of surface area and volume (12.74% and 30.52%, respectively), but the least variation in element number (10.08%). Additionally, we do not see any correlation with the time allocated to box modeling. The duration of modeling was more closely linked to the complexity of the original specimen; for example, the *Allosaurus* model required more time than the other models because of the presence of fenestrations, cavities, and other internal structures (not modeled in the vertebra and echinoderm fossils). Instead, the differences between the models largely reflect inaccuracies in the box-modeling process resulting from the limitations of using two-dimensional reference images (i.e., photographs or reconstructions) that show the

specimen in only a few orientations. The particularly high variation between the two *Allosaurus* models was due to the existence of large internal cavities, such as the endocranial space, which are difficult to model using two-dimensional templates. One way of mitigating these problems is to utilize photographs or reconstructions in multiple different views and cross-sections; the box-modeled *Stegosaurus* vertebra, which was based on photographs in five different orientations, was more similar to the digitized model (in terms of surface area and volume) than the *Allosaurus* and *Protocinctus* models (based on reconstructions in three and two different orientations, respectively) were to their respective CT-based models. However, published reference images (especially reconstructions) are frequently limited to just two or three different views of the specimen. Consequently, while box modeling can be used to broadly approximate morphology for the majority of fossils, it will often not be possible to accurately capture all anatomical details. Particular caution should be exercised when deriving measurements, including surface area and volume, from such models (without independent verification).

Another possible source of inaccuracies in box modeling results from the fact that the approach typically requires greater user input and interpretation than methods such as CT and photogrammetry (in particular), and is thus potentially much more subjective. This issue is likely to be particularly pronounced when modeling is based on published reconstructions (rather than photographs), as the different views might not correlate with one another. Subjectivity could be minimized by using high-quality photographs of specimens as reference images, studying and measuring original specimens, and seeking the guidance of researchers with expert knowledge of the anatomy of the specimens being modeled. Additionally, photographs and reconstructions must be scaled correctly prior to their use as guides for box modeling.

298

299   Regardless of these differences, the results of functional analyses (FEA and CFD) were  
300   qualitatively and quantitatively similar for the models generated using box modeling and the  
301   corresponding ones based on CT/photogrammetry (Figs. 4–6). Critically, the location and  
302   magnitude of peak stresses (FEA) and the velocity magnitudes and gradients (CFD) were  
303   very similar for each pair of models, albeit with some variation in the distributions of  
304   stresses/velocities. This means that possible interpretations of fossil functional performance  
305   derived from these analyses would be the same independent of the approach used to generate  
306   the model. The quantitative comparison between the results of the CFD simulations and the  
307   flume tank experiment (Fig. 6E–H) demonstrates that computational and physical models are  
308   capable of producing near identical fluid velocities near to fossil geometries. Moreover, the  
309   clear differences between these models and the CFD simulation of flow around a three-  
310   dimensional rectangle indicate that accurately representing the surface geometry is key to  
311   recovering flow patterns. Taken together, this implies that even though there were notable  
312   differences between the models depending on the approach taken (see above), these did not  
313   substantially alter the results of FEA or CFD.

314

315   This study indicates that box modeling can be used to produce 3-D models of fossils that are  
316   amenable to computational functional analyses, generating results that are almost identical to  
317   simulations for models based on CT or photogrammetry. As outlined in the introduction, box  
318   modeling has a number of advantages over tomographic and surface-based methods that  
319   make it particularly well-suited to paleontological functional analysis. The approach works  
320   well using ‘normal’ computers and free software, making it much cheaper than alternative  
321   techniques (that may require expensive instruments, computer hardware, and software).  
322   Additionally, box modeling can be quicker than digitally reconstructing specimens based on

CT datasets, which usually requires considerable time and user effort, especially when the fossil is hosted in rock (Cunningham et al., 2014; Sutton et al., 2014, in press). Digitizing specimens with photogrammetry is typically less time-consuming, but mounting, photographing, and digitally reconstructing fossils can still require several to tens of hours (Falkingham, 2012; Mallison and Wings, 2014). Perhaps more importantly, box modeling lends itself especially well to large-scale comparative studies of functional evolution, as it does not require that all the taxa to be included in the analysis are represented by complete, articulated specimens (unlike models based on digital reconstructions of fossils), just that suitable reference images are available (see above). Other possible applications include analyses of the functional performance of hypothetical morphologies, which could enable rigorous tests of evolutionary scenarios. Previous studies have used hypothetical models to investigate the functional significance of specific anatomical characters, such as the antorbital fenestrae in archosaurs (Rayfield and Milner, 2008), the tooth cingulum in mammals (Anderson et al., 2011b), and a range of hard- and soft-tissue structures in theropod dinosaurs (Lautenschlager et al., 2013; Lida et al., 2015). Although created with different software or partially based on models derived from the digitization of fossils, the possible questions that can be addressed using hypothetical models are equally applicable to box-modelled morphologies. There is also potential for combining methods such as CT and box modeling to virtually restore the morphology of fossil specimens distorted by taphonomy, enabling computational analyses of form and function (Cunningham et al., 2014).

Evidently, the study of digitally box-modeled specimens has great potential for informing studies of fossil functional morphology. As researchers continue to explore the applications of computational methods such as FEA and CFD, while becoming increasingly familiar with

open-source 3-D graphics and animations software, we anticipate that the integration of box modeling and functional analysis will soon become much more widespread in paleontology.

## ACKNOWLEDGEMENTS

I.A.R. was funded by an 1851 Royal Commission Research Fellowship. Paul Barrett (Natural History Museum, London), Charlotte Brassey (University of Manchester), and Emily Rayfield (University of Bristol) are thanked for providing datasets and digital models of *Allosaurus* and *Stegosaurus*. We thank two anonymous reviewers for their comments and the Paleontological Society for support.

## REFERENCES

- ANDERSON, P. S. L., J. A. BRIGHT, P. G. GILL, C. PALMER, and E. J. RAYFIELD. 2011. Models in palaeontological functional analysis. *Biology Letters*, 8(1):119–122. doi:10.1098/rsbl.2011.0674
- ANDERSON P. S. L., P. G. GILL, and E. J. RAYFIELD. 2011. Modeling the effects of cingula structure on strain patterns and potential fracture in tooth enamel. *Journal of Morphology*, 272(1):50–65. doi:10.1002/jmor.10896
- BATES, K. T., P. L. MANNING, B. VILA, and D. HODGETTS. 2008. Three-dimensional modelling and analysis of dinosaur trackways. *Palaeontology*, 51(4):999–1010. doi:10.1111/j.1475-4983.2008.00789.x
- BATES, K. T., P. L. MANNING, D. HODGETTS, and W. I. SELLERS. 2009. Estimating mass properties of dinosaurs using laser imaging and 3D computer modelling. *PLoS ONE*, 4(2):e4532. doi:10.1371/journal.pone.0004532
- BRASSEY, C. A., S. C. R. MAIDMENT, and P. M. BARRETT. 2015. Body mass estimates of an exceptionally complete *Stegosaurus* (Ornithischia: Thyreophora): Comparing

372 volumetric and linear bivariate mass estimation methods. *Biology Letters*,  
 373 11(3):20140984. doi:10.1098/rsbl.2014.0984  
 374 BREITHAUPT, B. H., N. A. MATTHEWS, and T. A. NOBLE. 2004. An integrated  
 375 approach to three-dimensional data collection at dinosaur tracksites in the Rocky  
 376 Mountain West. *Ichnos*, 11(1–2):11–26. doi:10.1080/10420940490442296  
 377 CUNNINGHAM, J.A., C.-W. THOMAS, S. BENGTSON, S. L. KEARNS, S. XIAO, F.  
 378 MARONE, M. STAMPANONI, and P. C. J. DONOGHUE. 2012. Distinguishing  
 379 geology from biology in the Ediacaran Doushantuo biota relaxes constraints on the  
 380 timing of the origin of bilaterians. *Proceedings of the Royal Society B*,  
 381 279(1737):2369–2376. doi:10.1098/rspb.2011.2280  
 382 CUNNINGHAM, J. A., I. A. RAHMAN, S. LAUTENSCHLAGER, E. J. RAYFIELD, and P.  
 383 C. J. DONOGHUE. 2014. A virtual world of paleontology. *Trends in Ecology &*  
 384 *Evolution*, 29(6):347–357. doi:10.1016/j.tree.2014.04.004  
 385 FALKINGHAM, P. L. 2012. Acquisition of high resolution three-dimensional models using  
 386 free, open-source, photogrammetric software. *Palaeontologia Electronica*, 15(1):1T.  
 387 GARWOOD, R. J., and J. A. DUNLOP. 2011. Morphology and systematics of  
 388 Anthracomartidae (Arachnida: Trigonotarbida). *Palaeontology*, 54(1):145–161.  
 389 doi:0.1111/j.1475-4983.2010.01000.x  
 390 GARWOOD, R. J., and J. A. DUNLOP. 2014. The walking dead: Blender as a tool for  
 391 paleontologists with a case study on extinct arachnids. *Journal of Paleontology*,  
 392 88(4):735–746. doi:10.1666/13-088  
 393 GIL, L., J. MARCÉ-NOGUÉ, and M. SÁNCHEZ. 2015. Insights into the controversy over  
 394 materials data for the comparison of biomechanical performance in vertebrates.  
 395 *Palaeontologia Electronica*, 18(1):10A.



396 GILES, S., M. I. COATES, R. J. GARWOOD, M. D. BRAZEAU, R. ATWOOD, Z.  
397 JOHANSON, and M. FRIEDMAN. 2015. Endoskeletal structure in *Cheirolepis*  
398 (Osteichthyes, Actinopterygii), an early ray-finned fish. *Palaeontology*, 58(5):849–  
399 870. doi:10.1111/pala.12182

400 GUNZ P., P. MITTEROECKER, S. NEUBAUER, G. W. WEBER, and F. L. BOOKSTEIN.  
401 2009. Principles for the virtual reconstruction of hominin crania. *Journal of Human*  
402 *Evolution*, 57(1):48–62. doi:10.1016/j.jhevol.2009.04.004

403 HAUG, J. T., A. MAAS, C. HAUG, and D. WALOSEK. 2011. *Sarotrocercus oblitus* – Small  
404 arthropod with great impact on the understanding of arthropod evolution? *Bulletin of*  
405 *Geosciences*, 86(4):725–736.

406 HAUG, C., D. E. G. BRIGGS, D. G. MIKULIC, J. KLUESSENDORF, and J. T. HAUG.  
407 2014. The implications of a Silurian and other thylacocephalan crustaceans for the  
408 functional morphology and systematic affinities of the group. *BMC Evolutionary*  
409 *Biology*, 14:159. doi:10.1186/s12862-014-0159-2

410 HESS, R., 2010. *Blender Foundations: The Essential Guide to Learning Blender 2.6*. Focal  
411 Press, Amsterdam, 404 p.

412 LAUTENSCHLAGER, S. 2014. Morphological and functional diversity in therizinosaur  
413 claws and the implications for theropod claw evolution. *Proceedings of the Royal*  
414 *Society B*, 281(1785):20140497. doi:10.1098/rspb.2014.0497

415 LAUTENSCHLAGER, S. 2015. Estimating cranial musculoskeletal constraints in theropod  
416 dinosaurs. *Royal Society Open Science*, 2(11):150495. doi:10.1098/rsos.150495

417 LAUTENSCHLAGER, S. In press. Digital reconstruction of soft-tissue structures in fossils.  
418 *In* L. TAPANILA and I. A. RAHMAN (eds.), *Virtual Paleontology*. The  
419 *Paleontological Society Papers*, XX.

420 LAUTENSCHLAGER, S., E. J. RAYFIELD, P. ALTANGEREL, L. E. ZANNO, and L. M.  
 421 WITMER. 2012. The endocranial anatomy of Therizinosauria and its implications for  
 422 sensory and cognitive function. PLoS ONE, 7(12):e52289.  
 423 doi:10.1371/journal.pone.0052289  
 424 LAUTENSCHLAGER, S., L. M. WITMER, P. ALTANGEREL, and E. J. RAYFIELD.  
 425 2013. Edentulism, beaks, and biomechanical innovations in the evolution of theropod  
 426 dinosaurs. Proceedings of the National Academy of Sciences of the United States of  
 427 America, 110(51):20657–20662. doi:10.1073/pnas.1310711110  
 428 LIDA, X., Y. WANG, E. SNIVELY, J. ZHANG, Z. DONG, M. E. BURNS, and P. J.  
 429 CURRIE. 2015. Model-based identification of mechanical characteristics of  
 430 *Sinosaurus* (Theropoda) crests. Acta Geologica Sinica, 89(1):1–11.  
 431 doi: 10.1111/1755-6724.12390  
 432 LIMAYE, A. 2012. Drishti: A volume exploration and presentation tool, 85060X. In S. R.  
 433 STOCK (ed.), Developments in X-Ray Tomography VIII. Proceedings of SPIE, 8506.  
 434 MADSEN, J. H. 1976. *Allosaurus fragilis*: A revised osteology. Utah Geological and  
 435 Mineralogical Survey Bulletin, 109:1–163.  
 436 MAIDMENT, S. C. R., C. BRASSEY, and P. M. BARRETT. 2015. The postcranial skeleton  
 437 of an exceptionally complete individual of the plated dinosaur *Stegosaurus stenops*  
 438 (Dinosauria: Thyreophora) from the Upper Jurassic Morrison Formation of Wyoming,  
 439 USA. PLoS ONE, 10(10):e0138352. doi:10.1371/journal.pone.0138352  
 440 MALLISON, H. and O. WINGS. 2014. Photogrammetry in paleontology – A practical guide.  
 441 Journal of Paleontological Techniques, 12:1–31.  
 442 PORRO, L. B., E. J. RAYFIELD, and J. A. CLACK. 2015. Descriptive anatomy and three-  
 443 dimensional reconstruction of the skull of the early tetrapod *Acanthostega gunnari*  
 444 Jarvik, 1952. PLoS ONE, 10(4):e0124731. doi:10.1371/journal.pone.0124731

445 RAHMAN, I. A., and S. ZAMORA. 2009. The oldest cinctan carpoid (stem-group  
 446 Echinodermata), and the evolution of the water vascular system. *Zoological Journal of*  
 447 *the Linnean Society*, 157(2):420–432. doi:10.1111/j.1096-3642.2008.00517.x  
 448 RAHMAN, I. A., J. A. WATERS, C. D. SUMRALL, and A. ASTOLFO. 2015a. Early post-  
 449 metamorphic, Carboniferous blastoid reveals the evolution and development of the  
 450 digestive system in echinoderms. *Biology Letters*, 11(10):20150776.  
 451 doi:10.1098/rsbl.2015.0776  
 452 RAHMAN, I. A., Z. BELAÚSTEGUI, S. ZAMORA, J. H. NEBELSICK, R. DOMÈNECH,  
 453 and J. MARTINELL. 2015b. Miocene *Clypeaster* from Valencia (E Spain): Insights  
 454 into the taphonomy and ichnology of bioeroded echinoids using X-ray micro-  
 455 tomography. *Palaeogeography, Palaeoclimatology, Palaeoecology*, 438:168–179.  
 456 doi:10.1016/j.palaeo.2015.07.021  
 457 RAHMAN, I. A., S. ZAMORA, P. L. FALKINGHAM, and J. C. PHILLIPS. 2015c.  
 458 Cambrian cinctan echinoderms shed light on feeding in the ancestral deuterostome.  
 459 *Proceedings of the Royal Society B*, 282(1818):20151964.  
 460 doi:10.1098/rspb.2015.1964  
 461 RAYFIELD, E. J. 2005. Using finite-element analysis to investigate suture morphology: A  
 462 case study using large carnivorous dinosaurs. *The Anatomical Record Part A*,  
 463 283A(2):349–365. doi:10.1002/ar.a.20168  
 464 RAYFIELD, E. J. 2007. Finite element analysis and understanding the biomechanics and  
 465 evolution of living and fossil organisms. *Annual Review of Earth and Planetary*  
 466 *Sciences*, 35:541–576. doi:10.1146/annurev.earth.35.031306.140104  
 467 RAYFIELD, E. J., D. B. NORMAN, C. C. HORNER, J. R. HORNER, P. M. SMITH, J. J.  
 468 THOMASON, and P. UPCHURCH. 2001. Cranial design and function in a large  
 469 theropod dinosaur. *Nature*, 409(6823):1033–1037. doi:10.1038/35059070

470 RAYFIELD E. J. and A. C. MILNER. 2008. Establishing a framework for archosaur cranial  
471 mechanics. *Paleobiology* 34(4):494–515. doi:10.1666/07006.1

472 RÜCKLIN, M., P. C. J. DONOGHUE, Z. JOHANSON, K. TRINAJSTIC, F. MARONE, and  
473 M. STAMPANONI. 2012. Development of teeth and jaws in the earliest jawed  
474 vertebrates. *Nature*, 491(7426):748–751. doi:10.1038/nature11555

475 SCHMIDT, D. N., E. J. RAYFIELD, A. COCKING, and F. MARONE. 2013. Linking  
476 evolution and development: Synchrotron radiation X-ray tomographic microscopy of  
477 planktic foraminifers. *Palaeontology*, 56(4):741–749. doi:10.1111/pala.12013

478 SHIINO, Y., O. KUWAZURU, Y. SUZUKI, and S. ONO. 2012. Swimming capability of the  
479 remopleuridid trilobite *Hypodicranotus striatus*: Hydrodynamic functions of the  
480 exoskeleton and the long, forked hypostome. *Journal of Theoretical Biology*, 300:29–  
481 38. doi:10.1016/j.jtbi.2012.01.012

482 SMITH, J. B., M. C. LAMANNA, H. MAYR, and K. J. LACOVARA. 2006. New  
483 information regarding the holotype of *Spinosaurus aegyptiacus* Stromer, 1915.  
484 *Journal of Paleontology*, 80(2):400–406. doi:10.1666/0022-  
485 3360(2006)080[0400:NIRTHO]2.0.CO;2

486 SMITH, S. Y., M. E. COLLINSON, P. J. RUDALL, D. A. SIMPSON, F. MARONE, and M.  
487 STAMPANONI. 2009. Virtual taphonomy using synchrotron tomographic  
488 microscopy reveals cryptic features and internal structure of modern and fossil plants.  
489 *Proceedings of the National Academy of Sciences of the United States of America*,  
490 106(29):12013–12018. doi:10.1073/pnas.0901468106

491 STEIN, M. 2010. A new arthropod from the early Cambrian of North Greenland, with a  
492 ‘great appendage’-like antennula. *Zoological Journal of the Linnean Society*,  
493 158(3):477–500. doi:10.1111/j.1096-3642.2009.00562.x

- SUTTON, M. D., R. J. GARWOOD, DAVID J. SIVETER, and DEREK J. SIVETER. 2012. SPIERS and VAXML; A software toolkit for tomographic visualisation and a format for virtual specimen interchange. *Palaeontologia Electronica*, 15(2):5T.
- SUTTON, M. D., I. A. RAHMAN, and R. J. GARWOOD. 2014. *Techniques for Virtual Palaeontology*. Wiley, Oxford, 208 p.
- SUTTON, M. D., I. A. RAHMAN, and R. J. GARWOOD. In press. Virtual paleontology – An overview. In L. TAPANILA and I. A. RAHMAN (eds.), *Virtual Paleontology. The Paleontological Society Papers*, XX.
- WITMER, L. M., S. CHATTERJEE, J. FRANZOSA, and T. ROWE. 2003. Neuroanatomy of flying reptiles and implications for flight, posture and behaviour. *Nature*, 425(6961):950–953. doi:10.1038/nature02048
- WU, C. 2013. Towards linear-time incremental structure from motion. *Proceedings of the 2013 International Conference on 3D Vision*:127–134. doi:10.1109/3DV.2013.25
- ZAPATA, U., K. METZGER, Q. WANG, R. M. ELSEY, C. F. ROSS, and P. C. DECHOW. 2010. Material properties of mandibular cortical bone in the American alligator, *Alligator mississippiensis*. *Bone*, 46(3):860–867. doi:10.1016/j.bone.2009.11.010
- ZELENITSKY, D. K., F. THERRIEN, and Y. KOBAYASHI. 2009. Olfactory acuity in theropods: Palaeobiological and evolutionary implications. *Proceedings of the Royal Society B*, 276(1657):667–673. doi:10.1098/rspb.2008.1075

## FIGURE CAPTIONS

FIGURE 1.—Box modeling a dorsal vertebra of the ornithischian dinosaur *Stegosaurus stenops* (NHMUK R36730) based on photographs of the original specimen in anterior and left lateral views (taken from Maidment et al., 2015). (A) Initial cube. (B) Subdivided cube. (C) Cube scaled to width of vertebral centrum. (D) Cube fitted to vertebral centrum in

anterior view by translating, rotating, extruding, and scaling elements. (E) Cube fitted to vertebral centrum in lateral view by translating, rotating, extruding, and scaling elements. (F, G) Further details (neural arch, zygapophyses, and neural spine) added in different aspects. (H) Final model in wireframe and solid views. Abbreviations: ancf, fossa surrounding neural canal on anterior surface; ri, ridge.

FIGURE 2.—3-D models of fossils generated using box modeling (A, C, E), or based on CT (B, F) or photogrammetry (D). (A, B) The skull of the theropod dinosaur *Allosaurus fragilis* (MOR 693). (C, D) A dorsal vertebra of the ornithischian dinosaur *Stegosaurus stenops* (NHMUK R36730). (E, F) A complete individual of the cinctan echinoderm *Protocinctus mansillaensis* (MPZ 2004/170).

FIGURE 3.—Results of CloudCompare analysis for 3-D models of fossils generated using box modeling or based on CT/photogrammetry. (A–C) False-color contour plots of the distances between elements for each pair of models. (A) The skull of the theropod dinosaur *Allosaurus fragilis* (MOR 693). (B) A dorsal vertebra of the ornithischian dinosaur *Stegosaurus stenops* (NHMUK R36730). (C) The cinctan echinoderm *Protocinctus mansillaensis* (MPZ 2004/170).

FIGURE 4.—Results of FEA for 3-D models of fossils generated using box modeling (A, C), or based on CT (B) or photogrammetry (D). (A–C) False-color contour plots of average Von Mises stress. (A, B) The skull of the theropod dinosaur *Allosaurus fragilis* (MOR 693). (C, D) A dorsal vertebra of the ornithischian dinosaur *Stegosaurus stenops* (NHMUK R36730). Red arrows indicate loads and orange triangles indicate constraints.

FIGURE 5.—Comparison of FEA results showing Von Mises stresses (A, D), deformation (B, E), and strain magnitudes (C, F). (A–C) A dorsal vertebra of the ornithischian dinosaur *Stegosaurus stenops* (NHMUK R36730). (D–F) The skull of the theropod dinosaur *Allosaurus fragilis* (MOR 693). Measurements were taken for selected points of the *Stegosaurus* vertebra (blue lines) and along the dorsal (blue lines) and lateral (red lines) surfaces of the *Allosaurus* skull. Solid lines indicate results of FEA for the models based on CT or photogrammetry and dotted lines indicate results of FEA for the models generated using box modeling.

FIGURE 6.—Results of computational and physical flow modeling for 3-D models of the cinctan echinoderm *Protocinctus mansillaensis* (MPZ 2004/170) generated using box modeling (A, C) or based on micro-CT (B, D). (A–D) False-color contour plots (horizontal and vertical cross-sections; ambient flow from left to right) of flow velocity magnitude. (E–H) Comparison of downstream velocity profiles for CFD simulations and physical modeling. Downstream velocity recorded at 0 mm (E), 10 mm (F), 20 mm (G), and 30 mm (H) downstream of the models. Green diamonds indicate results of CFD simulations for the model generated using box modeling, red circles indicate results of CFD simulations for the model based on a micro-CT scan, blue triangles indicate results of physical modeling, and magenta boxes indicate results of CFD simulations for the three-dimensional rectangle.

#### SUPPLEMENTAL DATA

SUPPLEMENTAL DATA 1.—3-D model (in STL format) of the skull of the theropod dinosaur *Allosaurus fragilis* (MOR 693) generated using box modeling.

568 SUPPLEMENTAL DATA 2.—3-D model (in STL format) of the skull of the theropod  
569 dinosaur *Allosaurus fragilis* (MOR 693) based on CT.

570

571 SUPPLEMENTAL DATA 3.—3-D model (in STL format) of a dorsal vertebra of the  
572 ornithischian dinosaur *Stegosaurus stenops* (NHMUK R36730) generated using box  
573 modeling.

574

575 SUPPLEMENTAL DATA 4.—3-D model (in STL format) of a dorsal vertebra of the  
576 ornithischian dinosaur *Stegosaurus stenops* (NHMUK R36730) based on photogrammetry.

577

578 SUPPLEMENTAL DATA 5.—3-D model (in STL format) of a complete individual of the  
579 cinctan echinoderm *Protocinctus mansillaensis* (MPZ 2004/170) generated using box  
580 modeling.

581

582 SUPPLEMENTAL DATA 6.—3-D model (in STL format) of a complete individual of the  
583 cinctan echinoderm *Protocinctus mansillaensis* (MPZ 2004/170) based on CT.

584



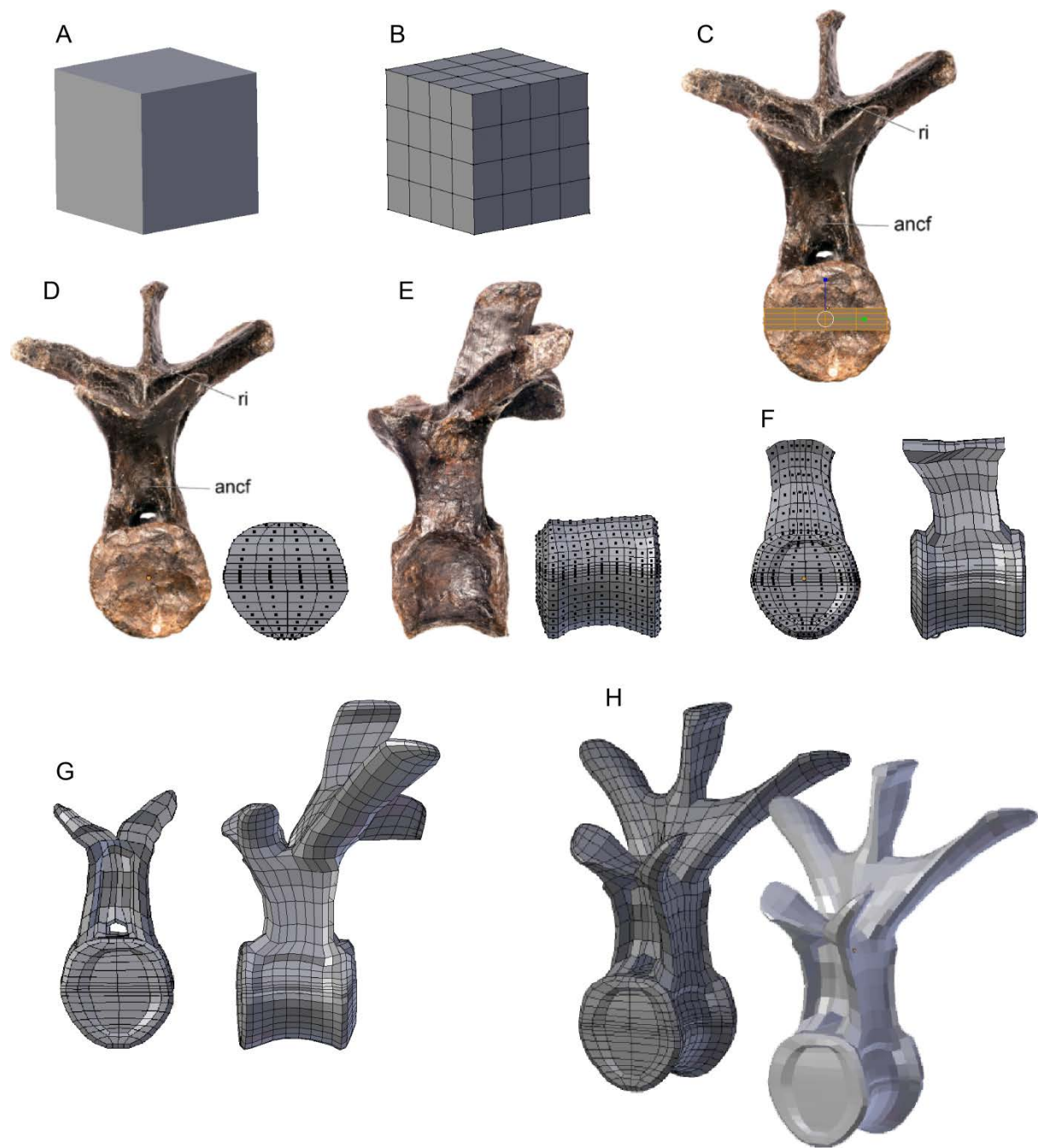


FIGURE 1.

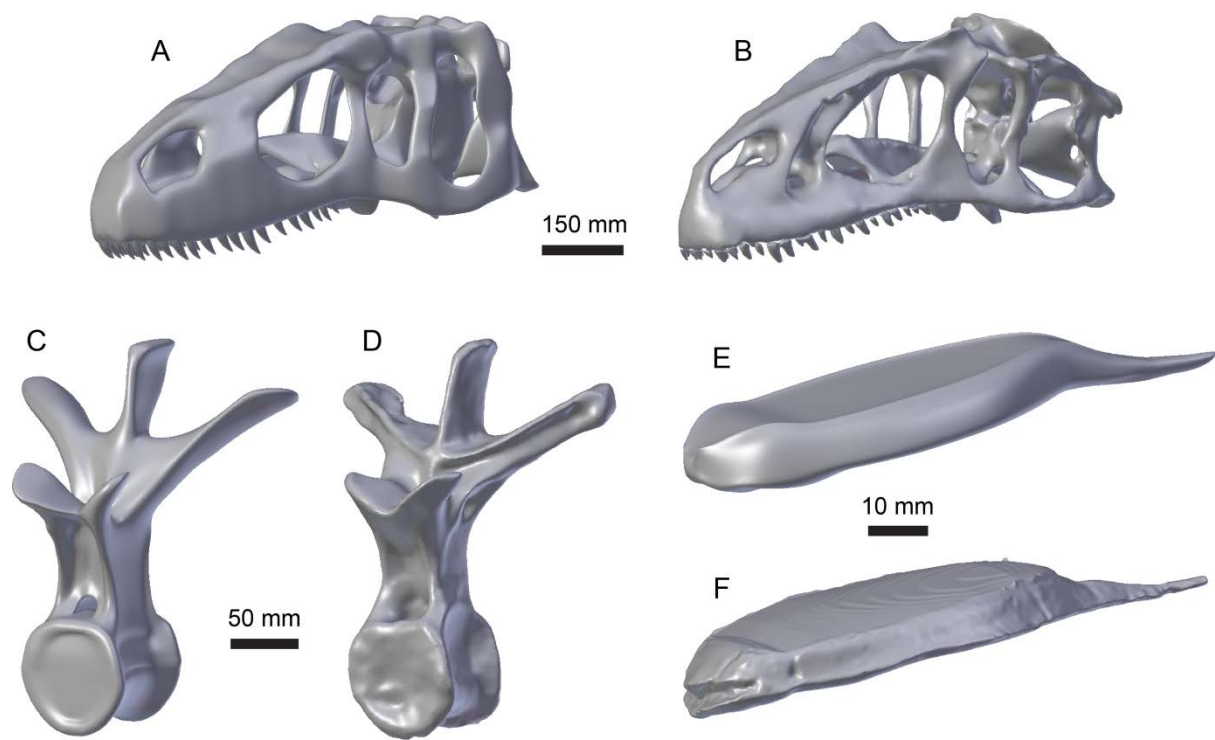


FIGURE 2.

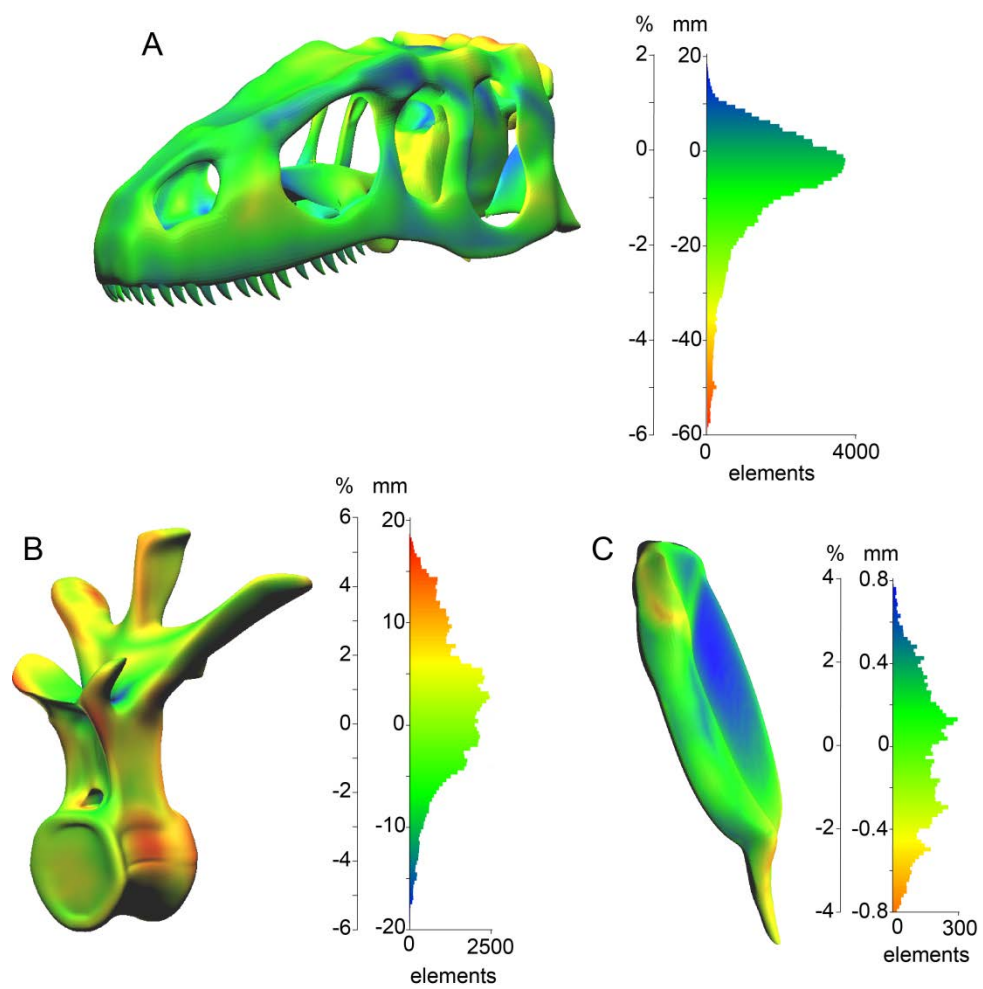


FIGURE 3.

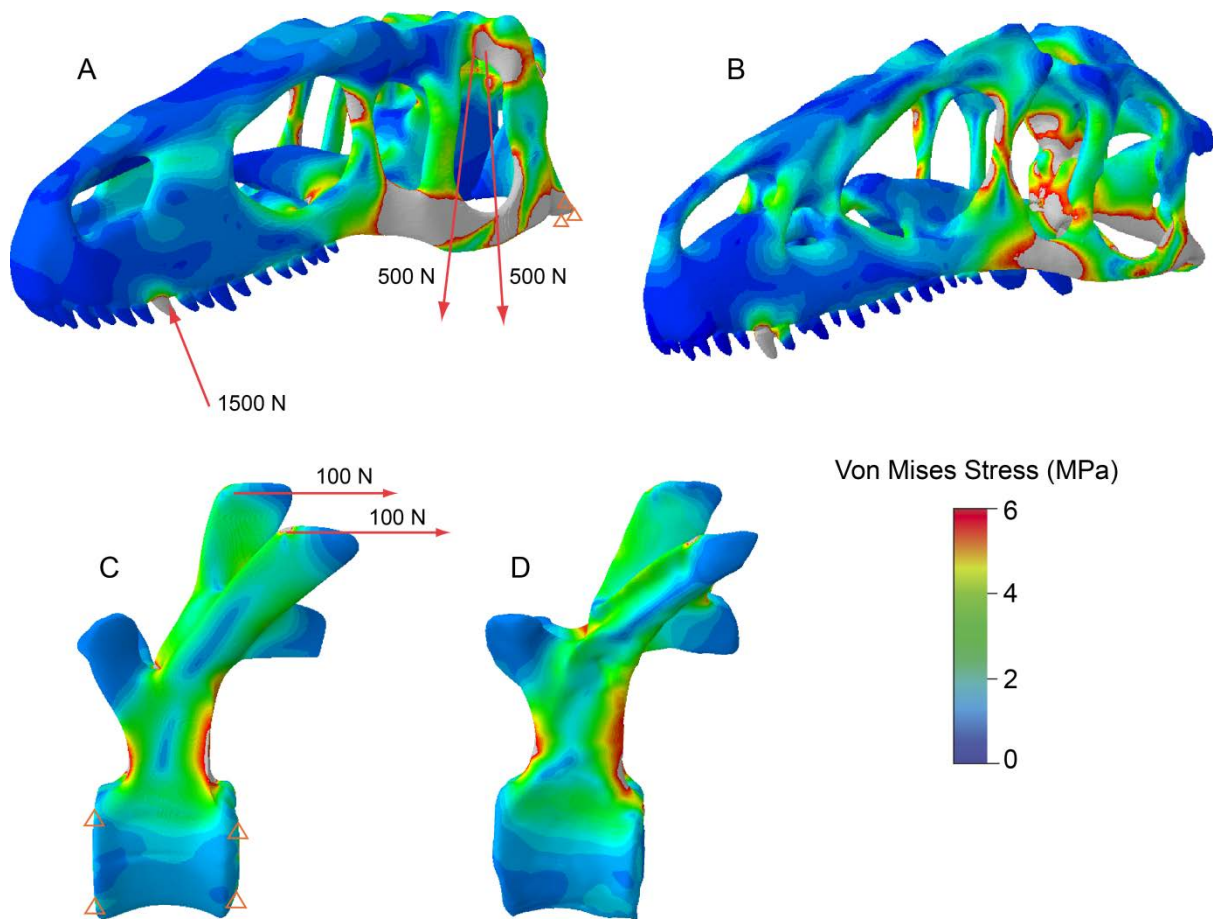


FIGURE 4.

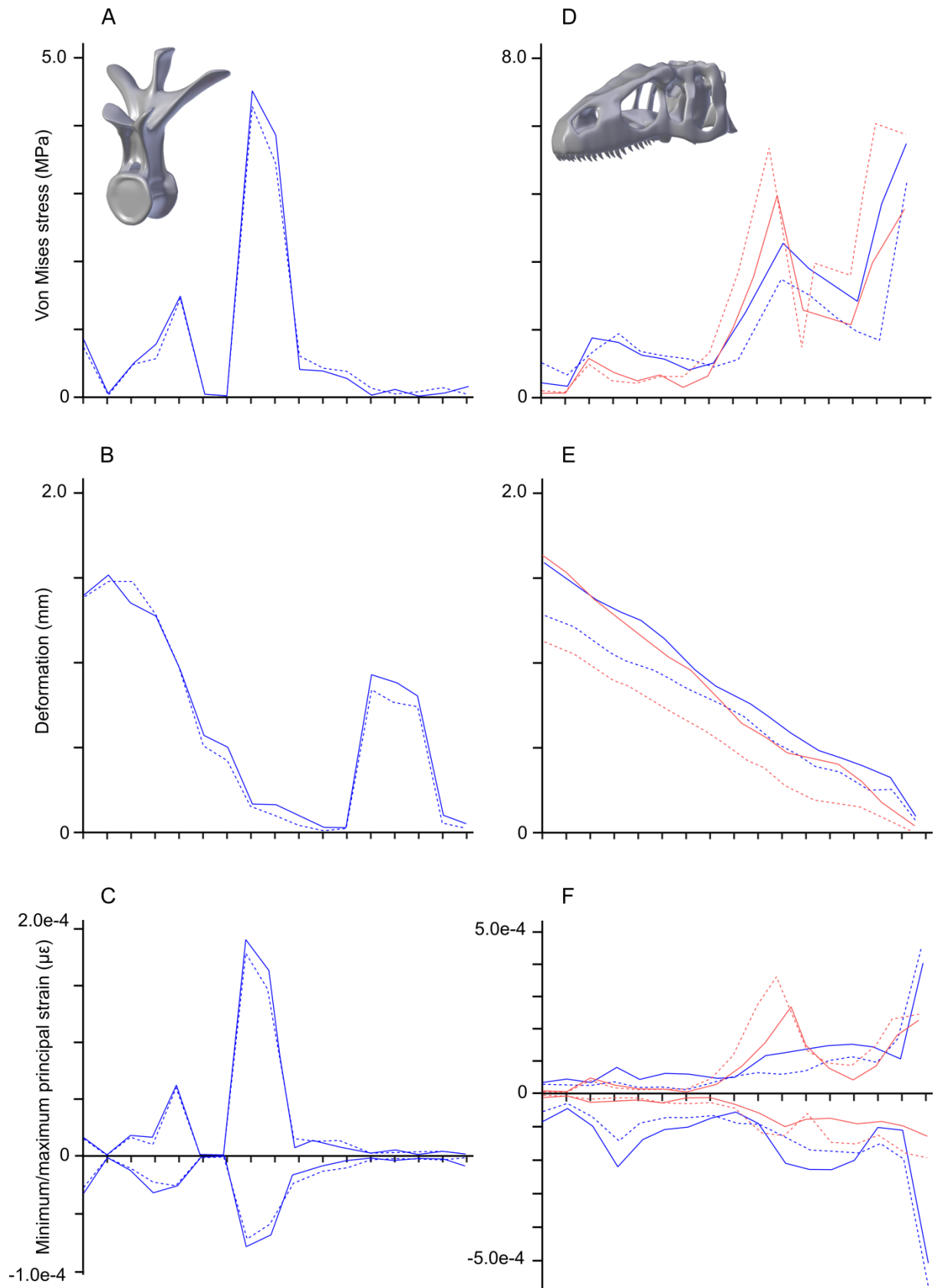


FIGURE 5.

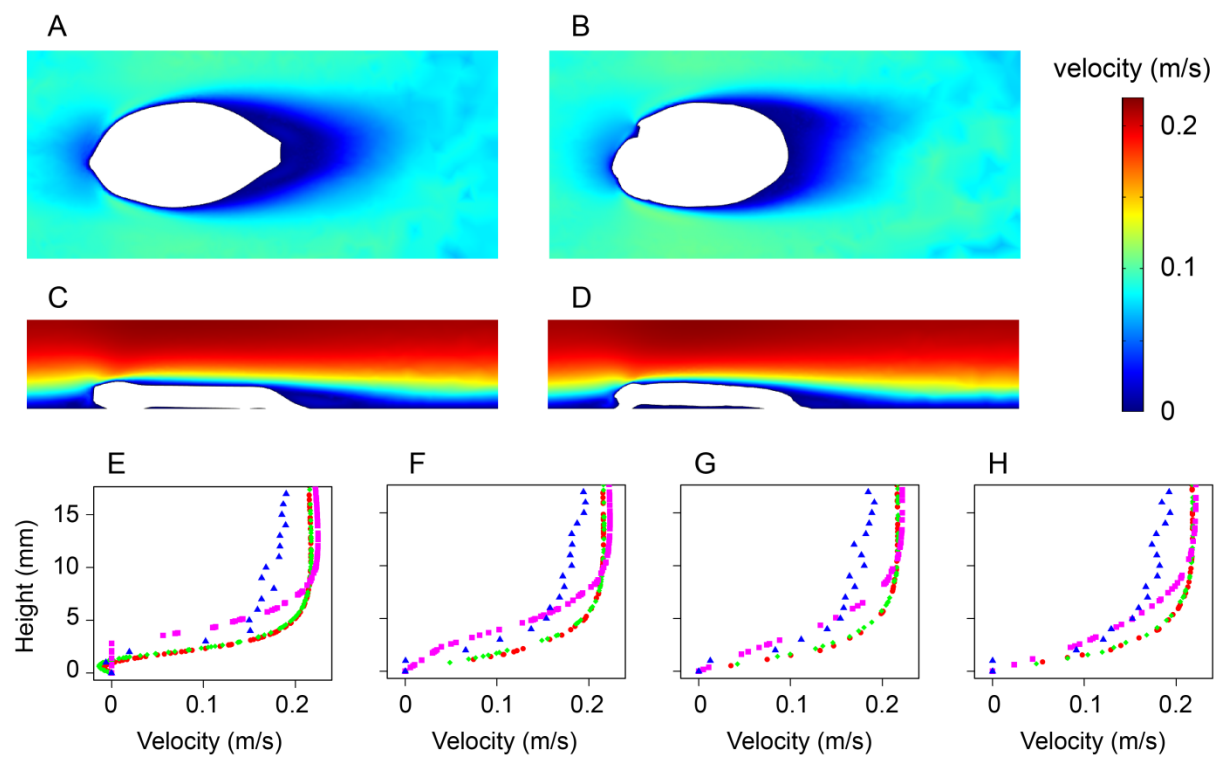


FIGURE 6.